Chemical Nature of Microfluidically Synthesized AuPd Nanoalloys Supported on TiO_2

Ghazal Tofighi[1,†], Xiaojuan Yu[2,†], Henning Lichtenberg[1,3], Dmitry E. Doronkin[1,3], Wu Wang[4], Christof Wöll[2], Yuemin Wang[2,], and Jan-Dierk Grunwaldt[1,3,*]*

[1] Institute for Chemical Technology and Polymer Chemistry (ITCP), Karlsruhe Institute of Technology (KIT), D-76131 Karlsruhe, Germany

[2] Institute of Functional Interfaces (IFG), Karlsruhe Institute of Technology (KIT), D-76344 Eggenstein-Leopoldshafen, Germany

[3] Institute of Catalysis Research and Technology (IKFT), Karlsruhe Institute of Technology (KIT), D-76344 Eggenstein-Leopoldshafen, Germany

[4] Institute of Nanotechnology (INT), Karlsruhe Institute of Technology (KIT), D-76344 Eggenstein-Leopoldshafen, Germany

ABSTRACT: Metal oxide supported bimetallic AuPd nanoparticles (NPs) are known to exhibit significantly enhanced activity and selectivity in numerous reactions compared to their monometallic counterparts. An atomic-level understanding of the nature of AuPd nanoalloys is among the most important and challenging topics in catalysis and nanoscience. Here, colloidal monometallic Au and Pd as well as bimetallic Au_xPd_y NPs (~1 nm) with different Au:Pd ratios were synthesized in a continuous microfluidic reactor and then deposited on TiO_2. The structural, electronic and reactive properties of Au_xPd_y/TiO_2 were first investigated by a multi-technique approach including scanning transmission electron microscopy, energy dispersive X-ray spectroscopy mapping, *in situ* X-ray absorption spectroscopy, FTIR spectroscopy, and X-ray photoelectron spectroscopy. Temperature-dependent IR spectroscopy using CO as a probe molecule provided deeper and solid evidence for the presence of a variety of active sites on the surface of monometallic Au and Pd NPs and Au_xPd_y nanoalloys. The results demonstrated consistently strong electronic interactions between Au and Pd upon alloying, leading to an interatomic charge transfer and electronic modifications in the d bands of Au and Pd. The $AuPd/TiO_2$ sample with an Au:Pd ratio of 3:7 exhibited the highest catalytic activity in CO oxidation compared to the other alloys. This was attributed to a synergistic effect where the activation of dioxygen is facilitated at the Pd-enriched sites while both bimetallic Au and Pd sites chemisorb CO. Hence, the combination of microfluidic synthesis and advanced characterization including FTIR allowed deeper insights into the nature of AuPd nanoalloys for catalytic applications.

1. Introduction

For a long time, the most noble among all metals, gold, was not expected to exhibit significant catalytic activity.[1-4] However, in the early 1990s Haruta et al. and then also other research groups[5] demonstrated that small Au nanoparticles (NPs) with diameters of 1-5 nm, deposited on suitable support materials, are active in low temperature CO oxidation[6-8] and selective oxidation of propylene to propylene oxide in the presence of oxygen and hydrogen.[9-10] Since then, catalytic properties of Au NPs have attracted much attention with respect to many applications such as water-gas shift (WGS) reactions[11-12], reduction of nitrogen oxides[13-14], oxidation of alcohols[5, 15], H_2O_2 synthesis from H_2 and O_2[11, 15], aerobic oxidation of alcohol[16-17], selective hydrogenation of alkenes[11] etc. Particle size affects two essential factors for the catalytic activity of supported gold NPs: the number of low-coordination sites and the total length of perimeter sites at the metal-support interfaces. So far, it has been difficult to unambiguously distinguish these two effects, and unraveling the importance of the individual contributions to the synergistic catalytic performance remains to be a major challenge. Additionally, quantum size effects resulting from confining the metal electrons and strain effects reducing the lattice constant of small metal particles may contribute to the chemical activity of ultrasmall metal particles.[1, 18-19]

Alternatively, various catalytic properties can be obtained by combining different metals to synthesize intermetallic compounds and nanoalloys.[20-21] Alloying often leads to synergistic effects resulting in higher catalytic activity, and the variety of alloys with different compositions, structures and properties gives many degrees of freedom to design bi- or trimetallic catalysts for particular applications, especially in the field of structure-sensitive reactions.[22-23] Bimetallic AuPd catalysts have been extensively applied for synthesis of vinyl acetate[24-25], H_2O_2[26-28] as well as alcohol and glucose oxidation.[29-32] Moreover, as Pd is already a key element in the well-established three-way catalyst due to its high CO oxidation activity at elevated

temperatures[33], addition of Pd to Au-based catalysts could be beneficial to improve the catalytic performance and durability of gold at high temperatures, while also inhibiting Au NP aggregation.[34-35] With respect to CO oxidation, several publications reported that O_2 dissociation, which in Au/TiO_2 takes place at the interface of Au and TiO_2[1, 8], could be facilitated by the presence of Pd. In some cases, such bimetallic systems were found to exhibit improved stability and higher catalytic activity at low temperatures compared to monometallic Au and Pd catalysts.[34-36] However, details of the involved mechanisms for charge transfer in small nanoalloys are still unclear. A deeper understanding requires a combination of well-defined homogeneous nanoalloy materials and advanced characterization techniques.

The homogeneity of the alloy particles, or the extent of segregation, is strongly influenced by the synthesis procedure and post-synthetic treatment such as precursors, temperature and pressure, and also on the nanoalloy composition. Within the interdisciplinary field of colloidal chemistry, NPs with tailored physical and chemical properties determined by particle size and shape can be synthesized.[20, 37] Apart from conventional-stirred batch reactors, microfluidic reactors equipped with micromixers are able to achieve homogeneous and efficient mixing of the reactants at a short time scales (ms). These advantages have attracted considerable attention in recent years, and microfluidic systems are of pronounced interest as novel, powerful devices to produce monometallic and alloyed NPs in a profoundly controlled manner. This allows tailoring particle sizes, structures (e.g. homogeneous nanoalloys, core-(multi)- shell and segregated subcluster structures), and achieving narrow size distributions of the nanoalloys, a requirement for further tuning the desired catalytic properties.[38-40]

Recently, we have studied the synthesis of Au and Pd NPs and also homogeneous Au_xPd_y nanoalloys inside a novel microfluidic reactor[41]. For the present study (note that this work was conducted in the frame of the PhD thesis by Ghazal Tofighi[42]), such bimetallic NPs were deposited on TiO_2, and the effects of alloying and Au-Pd interaction on surface properties. Next, the electronic structure and morphology were investigated using a multi-technique approach. Employing a novel ultrahigh-vacuum Fourier-transform infrared spectroscopy (UHV-FTIR) apparatus[43], a systematic *in situ* IR study using CO as probe molecule on Au/TiO_2, Pd/TiO_2, and Au_xPd_y/TiO_2 at different temperatures was conducted on these well characterized systems. The temperature-dependent FTIRS data in conjunctions with high-resolution XPS results provided new insights into the chemical nature of the Au-Pd interaction, allowing us to substantially advance the understanding of the mechanisms governing CO oxidation reactions on supported alloy particles.

2. Experimental Section

2.1 Materials

$HAuCl_4 \cdot 3H_2O$ (Roth, 99.5% purity), K_2PdCl_4 (Alfa Aesar, 99.99% purity), polyvinylpyrrolidone (Sigma-Aldrich, average molecular weight 40 kDa), $NaBH_4$ (Sigma-Aldrich, 99.99% purity), H_2SO_4 (Sigma-Aldrich, 95% purity) and TiO_2 (Evonik, commercially available Aeroxide P-25, anatase:rutile phase ratio of 80:20, surface area of 50 $m^2\ g^{-1}$) were used without further purification.

2.2. Microfluidic Reactor

In previous work[41, 44], we have introduced a novel microfluidic setup providing a continuous flow of reactants at high flow rates which was successfully employed to synthesize highly monodisperse and ultrasmall Au, Pd and AuPd NPs. The setup shown in Figure 1 features a fluid delivery rack and a microfluidic chip consisting of 3 cyclone micromixers and a meandering microchannel. A nitrogen gas pressure of 13 bar acts as a driving force for the flow of reactants stored in corrosion-resistant stainless steel vessels. The vessel for the metal precursor solution is coated with polyethylene. For each reactant, a flow rate of 1.3 L h^{-1} was applied to approach turbulent mixing conditions for the reactant flow in the micromixers with a Reynolds number of 2400 (total flow rate 2.6 L h^{-1}). This provides efficient mixing in 2 ms which is essential for such rapid reduction reactions. The total residence time of the reactants in the microfluidic device amounts to 20 ms. The microfluidic chip consists of Si-bonded glass. Inlet and outlet ports and the cylinders for the cyclone micromixers were produced by laser drilling. The meandering channel (cross section: 300 × 300 μm^2) was produced by Si etching. The design of the microfluidic chip also allows *in situ* characterization of the NPs during synthesis using spectroscopic and scattering techniques.

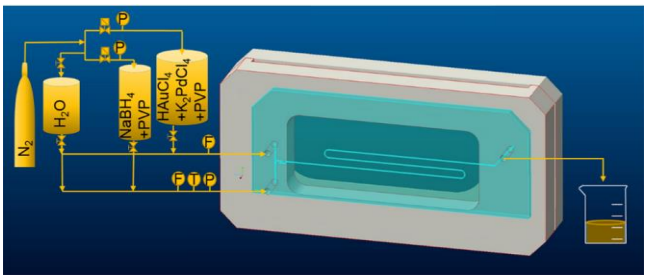

Figure 1. Schematic of the microfluidic setup including reactant vessels and microfluidic chip for synthesis of the metal NPs and nanoalloys in continuous flow (F, T and P: Flowmeter, temperature sensor and pressure transducer). The microfluidic chip made of Si-glass bonded wafer is sandwiched between the stainless steel support parts.

2.3. Microfluidic Synthesis of Au, Pd and AuPd Nanoparticles

Monometallic Au and Pd NPs as well as AuPd nanoalloys were synthesized following a previously published procedure[40-41]. In this colloidal route, the metal precursors are reduced under basic conditions (via $NaBH_4$) in the presence of PVP as a surfactant. Typically, an aqueous solution of mixed Au and Pd precursors (7.5 mM) with 666 mg PVP was prepared for all samples. The nominal molar Au:Pd ratio was 1:0, 7:3, 1:1, 3:7 and 0:1. A basic aqueous solution of $NaBH_4$ (37.5 mM) with 666 mg PVP was prepared as the reducing agent. These two solutions were poured separately into the corresponding vessels of the

microfluidic setup. A total flow rate of 2.6 L h^{-1} (turbulent regime) at 13 bar N_2 pressure (due to the high pressure drop) was used to push the reactants through the micromixers and the microchannel. Afterwards, the nanoparticles were collected in a flask and magnetically stirred for 1 h in an ice/water bath.

2.4. Preparation of Au/TiO_2, Pd/TiO_2 and $AuPd/TiO_2$ Catalysts

After dispersing 1 g TiO_2 in 80 mL distilled water in an ultrasonic bath, the colloidal NPs obtained from the microfluidic reactor were added to the suspension at room temperature and stirred for 1 h. Before impregnating TiO_2 with the NPs, the support was acidified with 0.1 mL pure H_2SO_4 solution (suspension pH: 2). Subsequently, the suspension was centrifuged 4 times (4500 rpm, 5 min each) and washed with H_2O in between. Finally, the catalysts were dried at 353 K overnight and calcined at 673 K for 3 h in static air. This method was applied for preparing 2.4 wt.% Au/TiO_2, Pd/TiO_2 and Au_xPd_y/TiO_2.

2.5. Characterization

2.5.1. Transmission Electron Microscopy

The catalyst powder samples were directly dispersed on Cu grids coated with holey carbon film. For colloid samples, 5 µl of the diluted colloidal solution was dropped on a holey carbon Cu grid covered with 2 nm carbon film and then dried at room temperature. Microstructure and morphology of the sample materials were investigated by high resolution transmission electron microscopy (HRTEM) and high angle annular dark-field (HAADF) scanning transmission electron microscopy (STEM). Composition was determined by energy dispersive X-ray spectroscopy (EDX) using an EDAX S-UTW EDX detector in a FEI Titan 80-300 microscope operating at 300 kV. Particle size statistics of the specimens were determined from the HAADF-STEM images by the ImageJ 1.49v software. Particle shaped were approximated with ellipsoids.[45] STEM-EDX data were analyzed by the TEM Image & Analysis (TIA 4.7 SP3 version) software.

2.5.2. X-Ray Absorption Near Edge Structure (XANES)

XANES spectra of Pd/TiO_2 and $AuPd/TiO_2$ pellets at the Pd K-edge (24.350 keV) were acquired at room temperature in transmission mode at CAT-ACT[46], a new wiggler beamline recently installed at the Karlsruhe Institute of Technology, using a Si (311) double crystal monochromator (beam size 1 × 1 mm^2) and ionization chambers. Higher harmonics were suppressed by a Rh-coated mirror downstream from the monochromator. Under the same conditions XANES data of the powder samples were acquired *in situ* (in quartz capillaries) under N_2 flow (33 ml min^{-1} flow rate) during heating to 673 K at 5 K min^{-1}. For raw data treatment the Athena program of the IFEFFIT software package[47] was used.

2.5.3. FTIR Spectroscopy and X-Ray Photoelectron Spectroscopy (XPS)

The FTIRS and XPS measurements were performed with a sophisticated ultra-high vacuum (UHV) setup, combing a vacuum FTIR spectrometer (Bruker Vertex 80v) and a multi-chamber UHV system (Prevac). This apparatus allows both IR reflection-absorption spectroscopy (IRRAS) on model systems and IR transmission on powders.[48-49] The Au_xPd_y/TiO_2 powder samples were first pressed into an inert metal grid and then mounted on a sample holder specifically designed for temperature-dependent FTIR transmission measurements. Prior to the IR measurements, the samples were pre-treated by annealing at 673 K for 1 h under UHV conditions. Oxidation states were monitored using an XPS apparatus equipped with a VG Scienta R4000 electron energy analyzer before IR measurements. Al K_α (nonmonochromatic, 1486.6 eV) radiation was used as excitation source. The energy resolution was better than 1 eV with a pass energy of 200 eV. The binding energies were calibrated based on the C1s line at 284.8 eV as a reference. The XP spectra were deconvoluted using the Casa XPS program with a Gaussian-Lorentzian mix function, a Doniach-Sunjic function for metallic Pd^0 species,[50] and Shirley background subtraction. For a quantitative analysis of the relative surface concentration of Au and Pd, sensitivity factors of 9.58 for Au $4f_{7/2}$ and 9.48 for Pd $3d_{5/2}$ were used.[51]

The TiO_2-supported metal particles were exposed to CO by using a leak-valve-based directional doser connected to a tube (inner diameter: 2 mm) terminating at a distance of 3 cm from the sample. IR spectra were recorded with a resolution of 4 cm^{-1} by using a spectrum of the clean sample as background reference. The temperature-dependent FTIR spectra were quantitatively analyzed by peak fittings in order to obtain normalized peak areas as a function of temperature.

2.5.4. CO Oxidation Test Procedure

CO oxidation was chosen as test reaction to assess the catalytic performance of the TiO_2 supported metal NPs. CO oxidation experiments were performed two times after two different pre-treatment procedures: exposure to N_2 at 673 K for 1 h and H_2 pre-treatment (5% H_2 in N_2) at 523 K for 1 h (10 K min^{-1} ramp rate in both cases). During the tests the catalysts were heated in a fixed-bed continuous-flow reactor (quartz tube, inner diameter 8 mm) in a temperature programmed mode from 303 K to 523 K at a ramp rate of 1 K min^{-1}. 70 mg of 2.4 wt.% Au_xPd_y/TiO_2 catalysts (sieve fraction 125–250 µm) were mixed with 930 mg SiO_2 and then fixed between glass wool plugs in the tube (catalyst bed length ~15 mm, gas flow 600 ml min^{-1}, gas hourly space velocity, GHSV: 48000 h^{-1}). The gas mixture contained 1000 ppm CO and 10% O_2 in nitrogen (CO feed rate: 5.8×10^{-6} mol s^{-1} g^{-1}_{cat}). The gas feed passed through a Messer Hydrosorb® cartridge to remove traces of water before reaching the reactor. Reaction products were analyzed using a URAS 10E NDIR CO/CO_2 analyzer. Each heating and cooling cycle was applied twice. Only the data acquired during the second cycle are shown in this paper. Turnover frequencies (TOFs) were calculated in the region between 3-17% CO conversion (for Au/TiO_2 below 40% in the temperature range of 323-336 K) and based on the assumption that the reaction rate (r) did not depend on the CO concentration.[8] For TOF calculations

the metal dispersion was estimated from mean NP diameters (determined by STEM).

3. Results and Discussion

3.1. Electron Microscopy and in situ XANES Spectroscopy under N_2 Flow

The different mono- and bimetallic NPs were all deposited on the same well-defined TiO_2 support in order to keep all parameters besides NP composition identical for comparability. STEM images allow characterizing particle shapes and sizes, as well as their aggregation, upon deposition and calcination. As an example, STEM images of colloidal Au_7Pd_3 NPs, supported/dried on TiO_2 and calcined sample with their corresponding histograms are shown in Figure S1. In this case, the average particle size increases from about 1 nm to 4 nm upon deposition on TiO_2 and further to 5 nm after calcination. A series of STEM images (Figure S2) shows the particle morphology and size distribution of NPs at different compositions deposited on TiO_2 after calcination at 673 K. The alloyed Au_xPd_y NPs, in particular the Au-rich alloys (Au_7Pd_3 and Au_5Pd_5) are notably smaller (5 and 6 nm) with narrower size distributions compared to Au/TiO_2 (11 nm). Due to low contrast in STEM image between oxidized Pd and the TiO_2 support in the calcined Pd/TiO_2 sample, the Pd NPs could not be unambiguously detected by electron microscopy. In case of Au_3Pd_7/TiO_2, precise determination of particle sizes is also difficult due to a segregated contiguous surface layer at the perimeter of the NPs on the support. STEM-EDX mapping (Figure 2) detected Pd in this segregated layer. Obviously, besides some Pd segregated out of the NPs, a certain amount of Pd is also located at the NP core together with Au, in accordance with the results of previous works.[41] The HRTEM images of calcined Au/TiO_2, Au_7Pd_3/TiO_2 and Au_3Pd_7/TiO_2 catalysts in Figure S3 reveal the atomic structure of Au, Au_7Pd_3 and Au_3Pd_7 NPs. The measured d-spacing of the (111) lattice planes within Au_7Pd_3/TiO_2 and Au_3Pd_7/TiO_2 catalysts is slightly smaller compared to Au/TiO_2 (d-spacing (111)=2.33 Å) indicating a presence of alloy structure of AuPd NPs.[41, 52] In the Au-rich alloys, Au and Pd are distributed uniformly in the NPs. STEM images and elemental mapping indicate that, under the applied preparation conditions, alloying reduces NP agglomeration compared to monometallic Au and Pd NPs, and additionally keeps the Pd with Au in the nanoparticles, which could influence the catalytic performance.

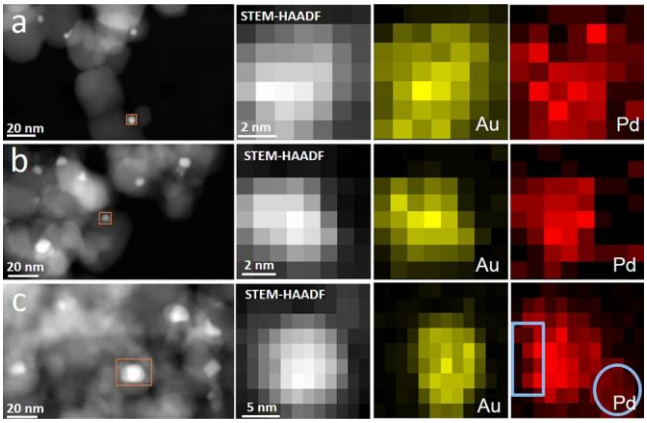

Figure 2. STEM-EDX mapping of calcined (a) Au_7Pd_3, (b) Au_5Pd_5 and (c) Au_3Pd_7 supported on TiO_2.

In order to determine the initial oxidation state of Pd in calcined Pd/TiO_2 and $AuPd/TiO_2$ catalysts and to monitor changes in oxidation state during the annealing treatment (UHV, heating up to 673 K for 1 h and cooling down to room temperature), the samples were investigated by *in situ* XANES spectroscopy under N_2 gas flow during heating up to 673 K and cooling down to room temperature. Figure S4 shows selected spectra acquired during heating. The results indicate that oxidized palladium dominates in both samples at all temperatures. A comparable trend was also observed during cooling. Figure S4 shows that the spectra of the NP samples clearly differ from the absorption data of a Pd foil representing metallic Pd (i.e. oxidation state zero). The same applies to the *ex situ* Pd K-edge XANES data of pellet samples (see Figure S5a) which also show that with increasing Au content in the alloyed NPs, Pd gets more reduced (in accordance with FTIR results in section 3.3). The corresponding Au L_3-edge in Figure S5b shows a lower whiteline intensity for the alloyed AuPd compared to the Au NPs, in accordance with literature.[41, 53]

3.2. XPS Data

Figure 3 shows Au 4f and Pd 3d XP spectra of various Au_xPd_y/TiO_2 samples (x:y = 1:0, 7:3, 1:1, 3:7, 0:1) pre-treated by annealing at 673 K for 1 h under UHV conditions. The monometallic Au/TiO_2 exhibits two spin–orbit components ($4f_{7/2}$ and $4f_{5/2}$) at 84.0 and 87.7 eV (Figure 3a), which are characteristic of the neutral Au^0 species; the corresponding Au $4d_{5/2}$ peak is located at 335.2 eV. For the pure Pd and all AuPd alloy samples, metallic Pd^0 was identified as majority species based on the dominating doublet at 335.3 (Pd $3d_{5/2}$) and 340.6 eV (Pd $3d_{3/2}$, Figure 3b). Additionally, the monometallic Pd and Pd-rich (70%) alloy NPs show another doublet at 337.1 and 342.4 eV, revealing the presence of some minority Pd^{2+} species.[54-57] It should be noted that in the core-level Pd 3d spectra, the relatively broad Au $4d_{5/2}$ peak at 335.2 eV is clearly resolved for the gold-rich (50% and 70%) alloys although it overlaps with the Pd $3d_{5/2}$ component.

On the basis of a quantitative analysis of the XPS data, the atomic ratios between Au and Pd were estimated. The results revealed a slightly higher Pd content for the

Au_xPd_y/TiO_2 samples when compared to the initial synthesis ratio (Table 1), indicating an enrichment of all alloy surfaces with Pd, in line with the literature.[24, 41] The concentration of Pd^{2+} was estimated as approx. 10% for monometallic Pd/TiO_2 and approx. 4.4% for Pd-enriched Au_3Pd_7/TiO_2. The Pd^{2+} species presumably result from activation of dioxygen at the surface of pure Pd and at the Pd-enriched sites of Au_3Pd_7/TiO_2. Indeed, in case of Au-rich (Au_5Pd_5/TiO_2 and Au_7Pd_3/TiO_2) samples, where the Pd atoms are incorporated as Pd^0 in an AuPd alloy structure, Pd^{2+} species were not observed. Alloying Au with Pd tends to shift the electron density toward the element with the larger fraction of empty valence states.[58] Figure 3a shows that for Au_3Pd_7/TiO_2 the Au 4f doublet shifts to lower binding energies (83.7 and 87.4 eV) upon alloying with Pd. This finding is attributed to the charge transfer from Pd to Au because Au is more electronegative.[34, 40, 59-60] The electronic interaction between Au and Pd in the alloy is of complex nature. It has also been proposed that Au gains *sp* valence electrons and loses *d* electrons whereas Pd loses *sp* electrons and gains *d* electrons.[58, 61-63] According to Wang et al., Au obtains 6s conduction charge in AuPd bimetallics accompanied by a slight 5d charge depletion.[64] The electronic perturbation in the *d* bands of Pd and Au was corroborated by the IR results shown below.

Table 1. Atomic Ratios of the Au_xPd_y/TiO_2 Based on XPS Results.

Sample	Au (%)	Pd (%)
Pd	0	100 (Pd^0 : Pd^{2+} = 90 : 10)
Au_3Pd_7	21.5	78.5 (Pd^0 : Pd^{2+} = 74.1 : 4.4)
Au_5Pd_5	36.6	63.4 (Pd^0)
Au_7Pd_3	56	44 (Pd^0)
Au	100	0

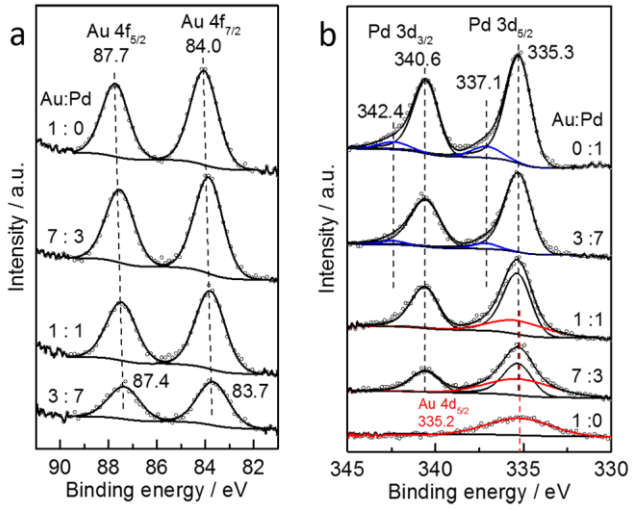

Figure 3. Deconvoluted X-ray photoelectron spectra of Au_xPd_y/TiO_2 samples (x:y = 1:0, 7:3, 1:1, 3:7, 0:1): (a) Au 4f region and (b) Pd 3d region.

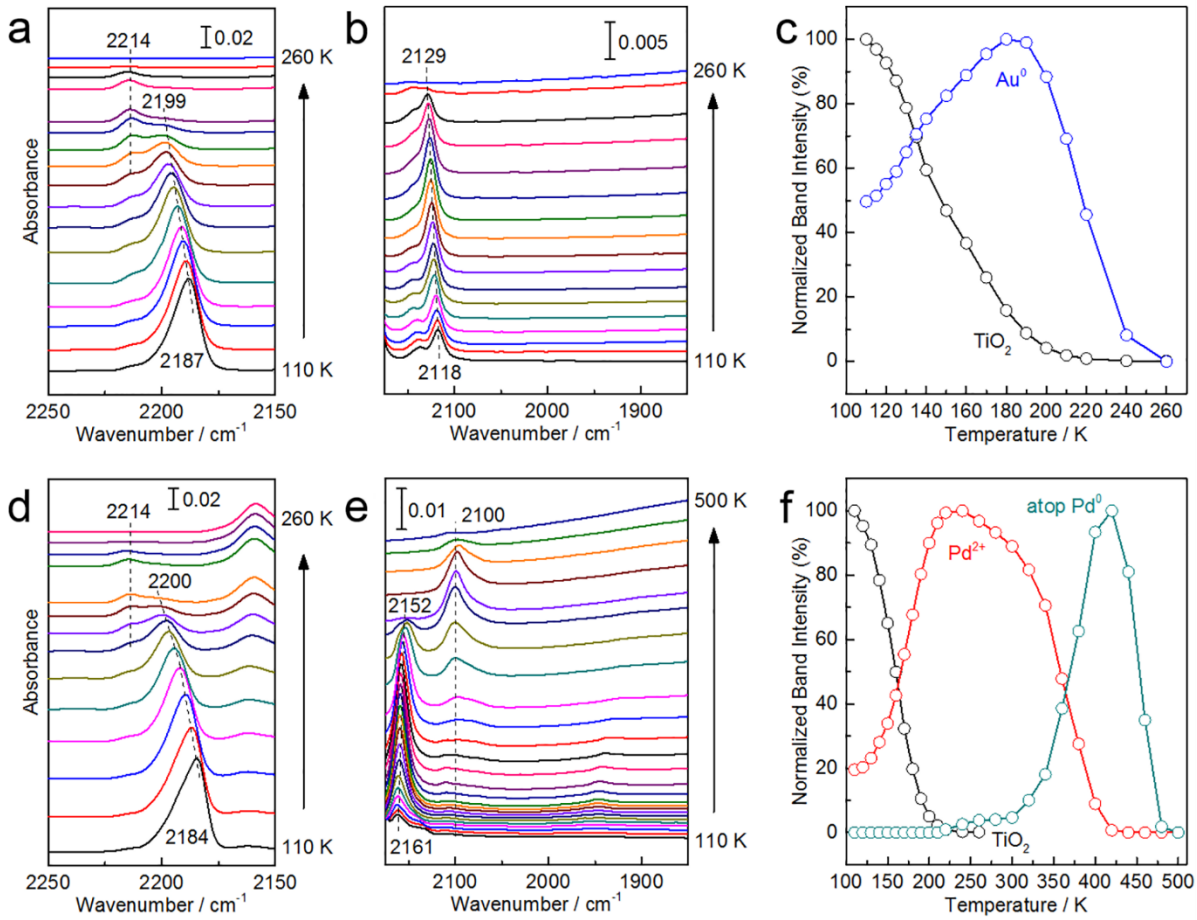

Figure 4. FTIR spectra recorded after exposing the Au/TiO_2 (a-c) and Pd/TiO_2 (d-f) samples to 4×10^{-3} mbar CO at 110 K and then heating gradually; (a, d) CO-TiO_2 region, (b) CO-Au region, (e) CO-Pd region and (c, f) normalized band intensity attributed to CO bound to different surface adsorption sites as a function of sample temperature.

3.3. Temperature-dependent FTIR Spectroscopy with CO as Probe Molecule

The surface properties and chemical states of various Au_xPd_y/TiO_2 samples were further characterized by FTIR spectroscopy using CO as a probe molecule (Figures 4 and 5). In contrast to XANES and XPS, the adsorbed CO speciesprobe exclusively metal species (Ti, Au, Pd) present at the very surface of the samples. For all TiO_2-supported catalysts, CO adsorption at 110 K caused the appearance of a predominant IR band at about 2185 cm^{-1}, which is assigned to CO bound to surface five-fold coordinated Ti^{4+} sites.[48] The large blue-shift with respect to the gas-phase value (2143 cm^{-1}) is related to both electrostatic interactions (Stark effect and Pauli repulsion) and electron donation from CO 5σ orbitals to the surface Ti^{4+} cations.[48] Interestingly, the frequency typical for CO bound in the vicinity of O-vacancies on TiO_2 surfaces for both, single crystals and powder particles at 2178 cm^{-1},[65] was not observed, suggesting that the TiO_2 particles were fully oxidized, in line with the XPS observations (see Figure S6). Based on the temperature-dependent IR data and assuming a pre-exponential factor of 10^{13} s^{-1},[66] the binding energy of CO was estimated as ca. 40 kJ mol^{-1}, revealing a rather weak interaction between CO and Ti^{4+}. The attenuation of the 2185 cm^{-1} band is accompanied by a slight blue-shift in frequency (from 2185 to 2200 cm^{-1}), which can be explained in terms of the reduced adsorbate-adsorbate interactions including both dynamic (dipole–dipole coupling) and substrate mediated static effects.[67] Interestingly, a weak CO band appears at 2214 cm^{-1} at elevated temperatures. This band shows a strongly enhanced thermal stability with regard to the CO species absorbed on regular Ti^{4+} sites (Figure 4a,d and 5a,d,g). This small band is tentatively assigned to a minority CO species coadsorbed with carbonates on the TiO_2 surfaces. A similar species has been reported in previous works for pure ZnO and Au/ZnO NPs.[68-69] The existence of carbonate anions, formed probably via CO oxidation, increases the Lewis acidity of adjacent Ti^{4+} cations. This effect accounts well for the unexpected enhancement of CO binding energy and the blue-shift of the ν(CO) band.[68-69]

3.3.1. CO Adsorption on Monometallic Au and Pd NPs Supported on Titania

Upon CO adsorption on pure Au NPs supported on TiO_2 at 110 K (see Figure 4a-c), in addition to the intense TiO_2-related CO vibration at 2185 cm^{-1}, a second IR band was observed at 2118 cm^{-1} being characteristic for CO adsorbed on Au sites.[19, 65, 70-74] The slight red-shift compared to the value of gas-phase CO (2143 cm^{-1}) is typical for CO bound to metals and is attributed to the electron back-donation

from Au to the empty CO 2π* orbital. Temperature-dependent FTIR data provide direct spectroscopic evidence of the thermal stability of different adsorbed species. As shown in Figure 4b,c, the 2118 cm^{-1} band increases first in intensity upon heating to 180 K. This could be related to (i) a restructuring process of the CO

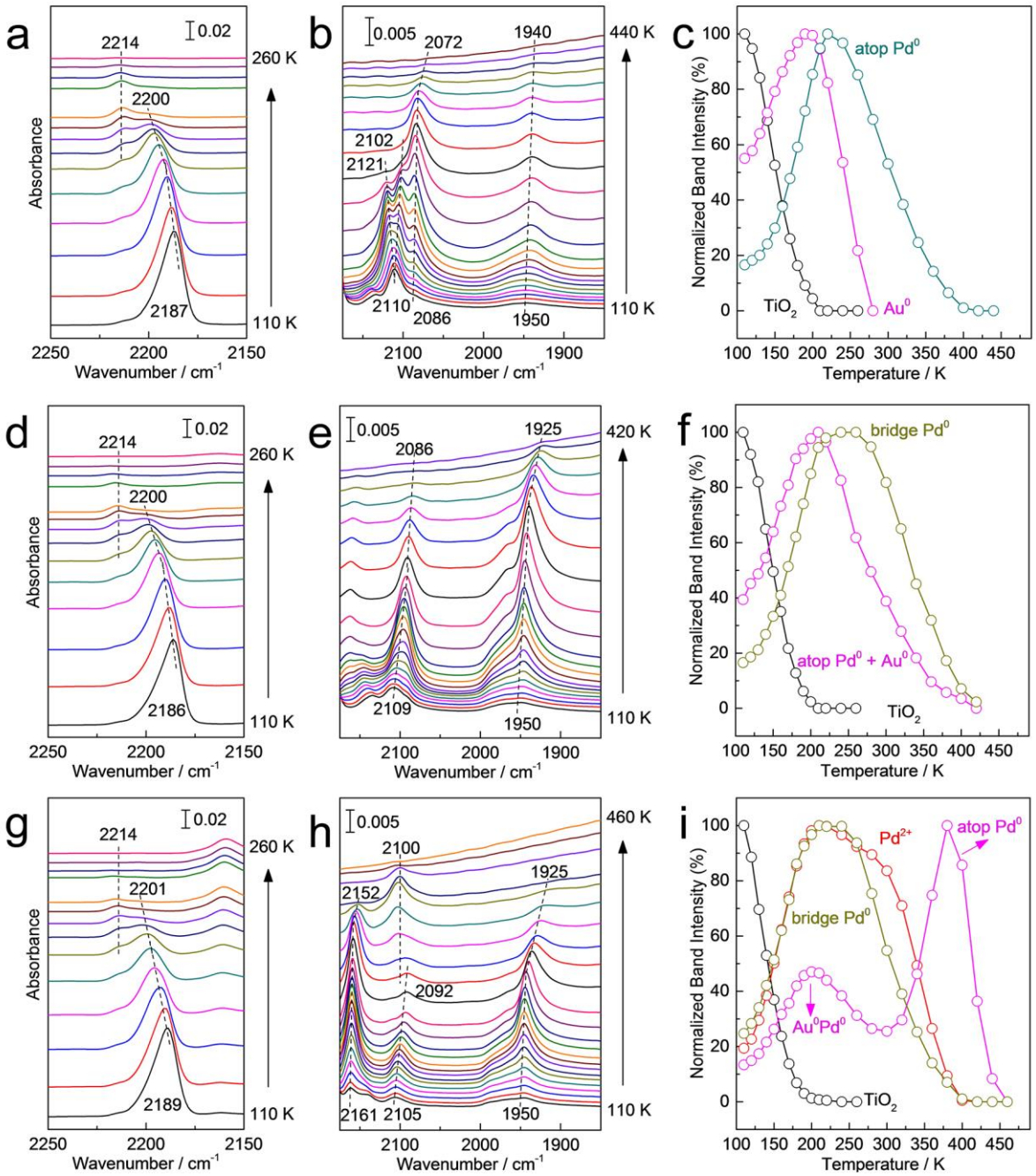

Figure 5. FTIR spectra recorded after exposing the Au_7Pd_3/TiO_2 (a-c), Au_5Pd_5/TiO_2 (d-f) and Au_3Pd_7/TiO_2 (g-i) samples to 4×10^{-3} mbar CO at 110 K and then subsequent gradual heating; (a, d, g) CO-TiO_2 region, (b, e, h) CO-AuPd region and (c, f, i) normalized band intensity of the CO bound to different surface adsorption sites as a function of sample temperature.

adlayer from an inhomogeneous distribution at low temperatures to a more uniform molecular environment and accordingly an increase in ordering and (ii) a thermal diffusion of CO adsorbed at Ti^{4+} sites to more stable Au sites.[75] Further rise of the temperature leads to a gradual attenuation of the Au-related CO band with a slight blue-shift in frequency from 2118 to 2129 cm^{-1}. According to previous works, the typical band of CO adsorbed on neu-

tral Au^0 sites appears at ~2100-2110 cm^{-1}.[19, 65, 72-74] The observed blue-shift for CO on Au/TiO_2 indicates an electronic modification of surface Au species which is probably caused by the strong interactions between Au atoms and the TiO_2 support at the interfacial sites. We propose that CO adsorbs preferentially at the low-coordinated Au sites at Au/TiO_2 interfaces. This CO species desorbs completely only after increasing the temperature to 260 K, in agreement with published studies.[19] The corresponding FTIR results obtained for Pd/TiO_2 are displayed in Figure 4d-f. CO adsorption at 110 K leads to the appearance of a new IR band at 2161 cm^{-1}, which is assigned to CO bound to positively charged Pd^{2+}. In fact, palladium is mostly oxidized as evidenced by *in situ* XANES and XPS results (cf. section 3.1 and 3.2, Figure S4a and Figure 3b). Upon temperature increase to 200 K (Figure 4e,f), the 2161 cm^{-1} band gains intensity in parallel to the desorption of CO on Ti^{4+} due to the same reasons as discussed above. The CO-Pd^{2+} species disappear as the temperature raises further. Interestingly, a weak IR signal at 2100 cm^{-1} appears and grows at temperatures above 300 K. It is known that CO molecules bound to specific surface Pd^0 sites show different vibrational frequencies: typically 2110-2070 cm^{-1} for linearly (on-top) bonded CO, 2000-1900 cm^{-1} for 2-fold bridging CO, and 1900-1800 cm^{-1} for CO adsorbed on 3-fold hollow sites.[24, 36, 76] Here, the band observed at 2100 cm^{-1} is characteristic for CO bound to Pd^0 atop sites. The intensity of this band reaches a maximum at 420 K, while at the same time the CO-Pd^{2+} species disappears. This observation suggests that the metallic Pd^0 is formed by the reduction of surface Pd^{2+} species via reaction with the CO, i.e. oxidizing the CO to CO_2 by consuming adjacent oxygen species.

3.3.2. CO Adsorption on Bimetallic Au_xPd_y (x:y = 7:3, 1:1, 3:7) NPs Supported on TiO_2

Figure 5a-c presents FTIR data obtained after CO adsorption on the bimetallic Au_7Pd_3/TiO_2 NPs at 110 K and then subsequently heating to higher temperatures. After exposure to CO at 110 K, one major IR band was observed at 2110 cm^{-1} in the Au-Pd region apart from the typical bands on titania, as already described above. As the sample temperature increased, the IR band at 2110 cm^{-1} was split into two components at 2121 and 2102 cm^{-1}, which are attributed to CO bound to Au^0 next to Pd in an on-top configuration and Au^0-enriched (contiguous) sites, respectively.[76] Both CO species desorbed completely upon heating to ~280 K, in line with the thermal stability of Au-bonded CO molecules. The Pd species coordinated to Au atoms can also be detected, they give rise to the IR feature at 2086 cm^{-1}. This frequency is attributed to CO adsorbed on-top of Pd^0 species. The 2086 cm^{-1} band disappeared only after heating to about 420 K, revealing that CO adsorbs stronger to Pd atoms than to Au. Furthermore, this band shifts to 2072 cm^{-1} with increasing temperature, i.e., with decreasing CO coverage (Figure 5b). The coverage-dependent frequency shift predominantly results from the adsorbate dipole-dipole coupling interactions, typically accompanying CO adsorption on metal surfaces.[77-78] The present IR data demonstrated that the Au_7Pd_3/TiO_2 surface was dominated by the bimetallic Pd^0 and Au^0 atoms whereas no CO-Pd^{2+} species was observed, in good agreement with the XPS results (see Table 1). Interestingly, on the surface of pure Pd NPs supported on TiO_2, only the CO frequency characteristic for positively charged Pd^{2+} was observed (Figure 4e). These findings suggest that on pure Pd NPs O_2 readily dissociates to form PdO_x, which is apparently absent on the alloy NPs. In addition, Figure 5b displays a weak and broad feature centered at 1940-1950 cm^{-1}, which is ascribed to CO adsorbed on bridge Pd sites, indicating the presence of a small amount of contiguous Pd ensembles on the surface.[24, 36, 76, 79]

As discussed in the XPS section, a net Pd to Au charge transfer is anticipated to occur upon alloying according to Pauling's electronegativity scale. However, this intermetallic charge transfer is partially compensated by the enrichment of Pd d-electrons and the depletion of Au d-electrons.[58, 61-63] Our IR data provides indirect information about modifications in the electronic structure of the bimetallic Au and Pd species. A lower Au d charge weakens the electron back-donation from Au into the CO $2\pi^*$ orbital and consequently strengthens the C–O vibration. In contrast, a red-shift of the CO-Pd^0 band takes place due to the charge transfer into the d bands of Pd. Indeed, the IR band of CO adsorbed on-top of bimetallic Pd sites was detected at 2086-2072 cm^{-1} (Figure 5b), which is obviously shifted to lower frequencies compared to that of CO bound to monometallic Pd atop sites (2100 cm^{-1}, Figure 4e). On the other hand, a blue-shift was observed for bimetallic Au-bonded CO (~2120 cm^{-1}) with respect to CO adsorbed at Au-enriched sites (2102 cm^{-1}, Figure 5b).

The IR spectra obtained after exposing Au_5Pd_5/TiO_2 to CO at 110 K show a broad band centered at ~2109 cm^{-1} in the Au-Pd region (Figure 5e), which is ascribed to mixed CO species adsorbed on bimetallic Au^0 and Pd^0 sites. Again, the intensity of this band reached the maximum at about 200 K and then gradually decreased with rising temperature, as observed for other samples (Figure 5e,f). At temperatures above 300 K, the CO band was red-shifted to 2086 cm^{-1} and disappeared at 420 K, corresponding to the more stable CO-Pd^0 species on the bimetallic surface. Additionally, compared with pure Pd (Figure 4e) and Au-rich alloy NPs (Figure 5b), the CO bound to Pd bridge sites becomes a dominating species as evidenced by the intense band at 1950-1925 cm^{-1}. This finding reveals the enrichment of the Au_5Pd_5/TiO_2 surface with Pd giving rise to contiguous Pd sites, where CO prefers to bind in a bridging configuration with a higher binding energy (Figure 5f). For this sample, the CO-Pd^{2+} species was observed only as a minority species, in line with the XPS results.

The FTIR data of CO adsorption on Pd-rich Au_3Pd_7/TiO_2 are presented in Figure 5g-i. In addition to the Ti^{4+}-related CO vibration, three intense bands at 2161, 2105 and 1950 cm^{-1} were observed after exposure to CO at 110 K (Figure 5h). They are attributed to CO adsorbed on positively charged Pd^{2+}, on-top of bimetallic Au^0 and Pd^0 sites, as well as bridging on Pd^0 sites in the Pd-enriched sample, respectively. These assignments are further supported by the thermal stability of various CO species, which is

demonstrated by the temperature-dependent IR experiments (Figure 5i). The attenuation of the CO band at ~2100 cm^{-1} at temperatures below 300 K originates predominantly from the desorption of CO-Au species because of a relatively weak bonding of CO to Au. Interestingly, this band shows a second maximum at 380 K, which is accompanied by a complete depletion of the CO-Pd^{2+} species (2161-2152 cm^{-1}), revealing the transformation of Pd^{2+} to Pd^{0} via CO oxidation (see above). As shown in Figure 5h, the corresponding IR band is located at ~2100 cm^{-1} being characteristic for CO bound in atop configuration on monometallic Pd^{0} sites, as observed for Pd/TiO_2 (Figure 4e). These results suggest the coexistence of Pd-enriched and bimetallic Au and Pd sites, in good agreement with the STEM-EDX results showing a segregated contiguous Pd layer around the alloy NPs (Figure 2). The enrichment of the surface with Pd was further supported by the intense CO band at 1950-1925 cm^{-1} originating from CO adsorbed on Pd bridge sites. The catalytic experiments (for details see below) provided evidence that the Pd-rich Au_3Pd_7/TiO_2 sample exhibited a higher CO oxidation activity compared to the other Au_xPd_y/TiO_2 catalysts. This could be related to a synergistic effect: the Pd-enriched (contiguous) sites activate dioxygen while CO chemisorbs on both bimetallic Au and Pd sites. It should be noted that the bimetallic Au sites bind CO weaker than Pd, which is expected to facilitate CO oxidation at low temperature as the self-poisoning effect can be diminished.

3.4. CO Oxidation with and without Reductive Pretreatment in H_2

Au/TiO_2, Pd/TiO_2 and $AuPd/TiO_2$ catalysts were tested with respect to CO oxidation in order to assess their catalytic performance in the reactor and to correlate it to the characterization results discussed above. First pre-treatment in N_2 up to 673 K for 1 h was applied in order to obtain conditions as close as possible to those during the FTIR measurements, and then the CO oxidation tests were performed. Afterwards, the samples were reduced in H_2 at 523 K for 1 h, and the CO oxidation tests were repeated under the same reaction conditions. Figure 6 and S7 shows the test results and the corresponding reaction rates (r). Pd/TiO_2 and $AuPd/TiO_2$ started to show low activity above 373 K, whereas the CO conversion over Au/TiO_2 was 30% at this temperature. Following a moderate light-off curve, Au/TiO_2 reached full CO conversion at around 500 K. Pd/TiO_2 and $AuPd/TiO_2$ catalysts showed a steeper rise in their activities and reached full conversion between 420-450 K (before Au/TiO_2). H_2 pre-treatment did not alter the observed trends, although, it improved the performance of the catalysts. Among the bimetallic samples, Au_3Pd_7/TiO_2 exhibited the best performance. This differ-

Table 2 Activation Energies, Turnover Frequencies and Temperature of 50% CO Conversion for CO Oxidation Tests.

Sample	After N_2 pre-treatment				After H_2 pre-treatment			
	E_a kJ mol^{-1}	TOF_{313K} s^{-1}	TOF_{393K} s^{-1}	$T_{50\%}$ K	E_a kJ mol^{-1}	TOF_{313K} s^{-1}	TOF_{393K} s^{-1}	$T_{50\%}$ K
Au/TiO_2	29	1.1	10.3	415	24	1.3	8.5	391
Au_7Pd_3/TiO_2	44	6.2×10^{-3}	1.9×10^{-1}	435	38	1.5×10^{-2}	3.0×10^{-1}	417
Au_5Pd_5/TiO_2	77	3.0×10^{-4}	1.1×10^{-1}	428	56	3.5×10^{-3}	2.8×10^{-1}	408
Au_3Pd_7/TiO_2	50	8.7×10^{-3}	4.3×10^{-1}	412	50	1.2×10^{-2}	6.2×10^{-1}	402
Pd/TiO_2	47	6.1×10^{-3}	2.5×10^{-1}	428	39	1.7×10^{-2}	3.7×10^{-1}	413

ence was more pronounced when only N_2 had been used for the pre-treatment. Reduction of oxidized metal nanoparticles with H_2 enhanced the activities of Au_5Pd_5/TiO_2, Au_7Pd_3/TiO_2 and Pd/TiO_2 more significantly compared to the Au_3Pd_7/TiO_2. The turnover frequencies (TOFs) calculated for the catalysts at 313 K (extrapolated from Arrhenius plots) and 393 K are given in Table 2. The TOFs disclose a gradual increase in the order of Au_5Pd_5/TiO_2 < Pd/TiO_2 ≤ Au_7Pd_3/TiO_2 < Au_3Pd_7/TiO_2 < Au/TiO_2. Apparent activation energies decreased in the order of Au_5Pd_5/TiO_2 > Au_3Pd_7/TiO_2 ≥ Pd/TiO_2 ≥ Au_7Pd_3/TiO_2 > Au/TiO_2.Reductive pretreatment increased the CO oxidation rate and decreased the activation energy E_a. This may be explained by O vacancies (O_v) created in the reducible titania support.[80] O_v can have a two effects: on the one hand O_v facilitate dissociative adsorption of O_2, and, on the other hand, they can stronger bind adsorbed CO.[81] It is well-known that CO oxidation to CO_2 on metallic clusters is governed by adsorption and dissociation of O_2 and the binding strength of CO.[82-83] Since the activation energy of CO oxidation over Au_5Pd_5/TiO_2 and Au_7Pd_3/TiO_2 decreased after reductive pretreatment we believe that CO poisoning[84] is also decreased (which would contradict stronger adsorption of CO on O_v of TiO_2), therefore dissociation of O_2 is rate limiting in this case, similar to the route proposed for Au/CeO_2.[85-86] A lower degree of CO poisoning on AuPd alloys compared to pure Pd in the temperature range of interest is supported by the FTIR data (compare Figure 4f with Figure 5c,f,i) and first-principles calculations.[87] The catalyst showing the highest synergetic effect of Au and Pd (both with and without reductive activation) is exactly the one which shows partial segregation of Pd. Even after the reductive pretreatments monometallic Pd^0 entities would be oxidized to PdO under CO and O_2 feed (which is net-oxidizing). Pd is known to be rapidly reoxidized in the presence of oxygen at intermediate temperatures, i.e. the reductive activation does not stabilize Pd^0 in the oxidizing atmosphere.[88] Pd-enriched (contiguous) sites are highly active in dissociative adsorption of O_2 while bimetallic AuPd sites also present in the catalyst are responsible for adsorption of CO without being poisoned at the same time. The activation energies and turnover frequencies over Au_3Pd_7/TiO_2 are practically not influenced by the reductive activation. This indicates that O_2 activation in this sample occurs on Pd-enriched sites.

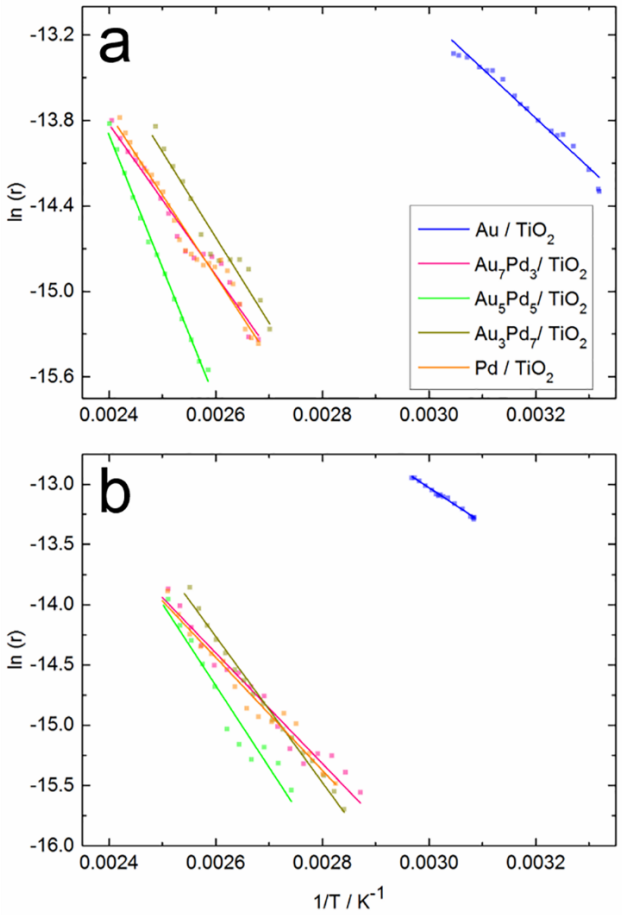

Figure 6. Arrhenius plots for CO oxidation over Au/TiO_2, Au_3Pd_7/TiO_2, Au_5Pd_5/TiO_2, Au_7Pd_3/TiO_2 and Pd/TiO_2 catalysts after (a) N_2 and (b) H_2 pre-treatment. Conditions: 1000 ppm CO, 10% O_2 in N_2, GHSV: 48000 h^{-1} and 1 K min^{-1} ramp rate.

These results indicate synergistic effects in the AuPd bimetallic catalysts at higher temperatures, with Au_3Pd_7/TiO_2 exhibiting the highest CO oxidation activity due to AuPd alloyed NPs responsible for adsorption of CO without being poisoned and activation of O_2 molecules by the Pd^{2+} species. These results confirm the anticipation based on temperature-dependent FTIR data regarding the catalytic performance of such samples.

4. Conclusions

Ultrasmall Au_xPd_y (x:y = 1:0, 7:3, 1:1, 3:7 and 0:1) NPs with average diameters of ~ 1 nm were synthesized in a continuous turbulent flow using a microfluidic reactor. The Au_xPd_y NPs supported on TiO_2 (P-25) showed some level of aggregation upon deposition, drying and calcination. However, the alloyed Au_xPd_y/TiO_2 (especially the Au-rich alloys) showed a narrower size distribution with an average diameter of ca. 5 nm. STEM images and EDX mapping revealed a Pd segregated contiguous layer in the Pd-rich alloy (Au_3Pd_7). Interestingly, this sample showed the highest synergistic effect in CO oxidation tests compared to the other bimetallic samples with a steep rise in their

activities surpassing Au/TiO_2. *In situ* XANES spectra of the Pd/TiO_2 and $AuPd/TiO_2$, proved the dominance of oxidized Pd at temperatures between 298 and 673 K under N_2 flow.

The different surface (active) sites (Ti^{4+}, Pd^{2+}, Au^0, atop Pd^0 and bridge Pd^0) of monometallic and bimetallic AuPd NPs dispersed on TiO_2 powders were identified by temperature-dependent FTIR spectroscopy using CO as a probe molecule. The surfaces of pure Au and Pd particles mostly consists of neutral Au and positively charged Pd^{2+}, respectively. Upon alloying, the bimetallic Au^0 and Pd^0 sites become the major surface species while depending on the Au:Pd ratio, the Au-enriched and Pd-enriched components were also detected. The combined IR and XPS results demonstrated strong electronic interactions between Au and Pd, which likely result from an interatomic charge transfer and electronic modifications in the d bands of Au and Pd. A synergistic effect accounts for the higher activity of the Au_3Pd_7/TiO_2 sample for CO oxidation to CO_2, in which the Pd-enriched sites are responsible for the activation of molecular oxygen while both bimetallic Au and Pd sites chemisorb CO. The interaction between metal NPs and support is known to play a crucial role in NP stabilization and the catalytic performance. The titania phase, surface crystallographic plane and defects are crucial parameters.[89-90] The influence of TiO_2 support on the catalytic activity of AuPd nanoalloys would thus be an interesting topic for future studies.

AUTHOR INFORMATION

Corresponding Authors

* E-mail: yuemin.wang@kit.edu (Y.W.)
* E-mail: grunwaldt@kit.edu (J.-D.G.)
Tel.: +49 721 608-42120
Fax: +49 721 608-44820

Author Contributions

The manuscript was written through contributions of all authors. All authors have given approval to the final version of the manuscript. †(G.T.) and (X.Y.) contributed equally.

Funding Sources

Virtual Institute VI-403 "In-situ Nano Imaging of Biological and Chemical Processes";
BMBF (projects 05K10VK1, 05K13VK2);
"Science and Technology of Nanosystems" Programme (432202)
China Scholarship Council

ASSOCIATED CONTENT

Supporting Information. Nanoparticle aggregation during deposition on supports and calcination. STEM images and size distributions of Au_xPd_y/TiO_2. HRTEM images of supported nanoparticles on titania. *In situ* and *ex situ* XANES spectra, XPS data, CO oxidation tests.

ACKNOWLEDGMENTS

The Virtual Institute VI-403 "In-situ Nano Imaging of Biological and Chemical Processes", the BMBF (projects 05K10VK1, 05K13VK2), "Science and Technology of Nanosystems" Programme (432202) and KIT are gratefully acknowledged for financial support. In addition, we would like to appreciate the Karlsruhe Nano Micro Facility (KNMF), a Helmholtz research infrastructure at KIT for providing STEM-EDX measurements. Xiaojuan Yu thanks the PhD fellowships sponsored by the China Scholarship Council. Finally, we thank the CAT-ACT beamline at the KIT synchrotron for providing beamtime, in particular Dr. Tim Prüßmann and Dr. Anna Zimina (IKFT) for their help and technical support during XAS experiments.

REFERENCES

(1) Yao, Q.; Wang, C.; Wang, H.; Yan, H.; Lu, J. Revisiting the Au Particle Size Effect on TiO_2-Coated Au/TiO_2 Catalysts in CO Oxidation Reaction. *J. Phys. Chem. C* **2016,** 120, 9174-9183.

(2) Zwijnenburg, A.; Goossens, A.; Sloof, W. G.; Crajé, M. W.; van der Kraan, A. M.; Jos de Jongh, L.; Makkee, M.; Moulijn, J. A. XPS and Mössbauer Characterization of Au/TiO_2 Propene Epoxidation Catalysts. *J. Phys. Chem. B* **2002,** 106, 9853-9862.

(3) Hammer, B.; Norskov, J. Why Gold is the Noblest of All the Metals. *Nature* **1995,** 376, 238-240.

(4) Meyer, R.; Lemire, C.; Shaikhutdinov, S. K.; Freund, H.-J. Surface Chemistry of Catalysis by Gold. *Gold Bull.* **2004,** 37, 72-124.

(5) Villa, A.; Wang, D.; Su, D. S.; Prati, L. New Challenges in Gold Catalysis: Bimetallic Systems. *Catal. Sci. Technol.* **2015,** 5, 55-68.

(6) Haruta, M.; Tsubota, S.; Kobayashi, T.; Kageyama, H.; Genet, M. J.; Delmon, B. Low-Temperature Oxidation of CO over Gold Supported on TiO_2, α-Fe_2O_3, and Co_3O_4. *J. Catal.* **1993,** 144, 175-192.

(7) Haruta, M.; Yamada, N.; Kobayashi, T.; Iijima, S. Gold Catalysts Prepared by Coprecipitation for Low-Temperature Oxidation of Hydrogen and of Carbon Monoxide. *J. Catal.* **1989,** 115, 301-309.

(8) Tsubota, S.; Nakamura, T.; Tanaka, K.; Haruta, M. Effect of Calcination Temperature on the Catalytic Activity of Au Colloids Mechanically Mixed with TiO_2 Powder for CO Oxidation. *Catal. Lett.* **1998,** 56, 131-135.

(9) Haruta, M.; Uphade, B.; Tsubota, S.; Miyamoto, A. Selective Oxidation of Propylene over Gold Deposited on Titanium-Based Oxides. *Res. Chem. Intermediat.* **1998,** 24, 329-336.

(10) Uphade, B.; Tsubota, S.; Hayashi, T.; Haruta, M., Selective Oxidation of Propylene to Propylene Oxide or Propionaldehyde over Au Supported on Titanosilicates in the Presence of H_2 and O_2. *Chem. Lett.* **1998,** 27, 1277-1278.

(11) Hashmi, A. S. K.; Hutchings, G. J. Gold Catalysis. *Angew. Chem. Int. Ed.* **2006,** 45, 7896-7936.

(12) Sandoval, A.; Gómez-Cortés, A.; Zanella, R.; Díaz, G.; Saniger, J. M. Gold Nanoparticles: Support Effects for the WGS Reaction. *J. Mol. Catal. A Chem.* **2007,** 278, 200-208.

(13) Ueda, A.; Oshima, T.; Haruta, M. Reduction of Nitrogen Monoxide with Propene in the Presence of Oxygen and Moisture over Gold Supported on Metal Oxides. *Appl. Catal. B Environ.* **1997,** 12, 81-93.

(14) Bollinger, M. J.; Sievers, R. E.; Fahey, D. W.; Fehsenfeld, F. C. Conversion of Nitrogen Dioxide, Nitric Acid, and n-Propyl Nitrate to Nitric Oxide by a Gold-Catalyzed Reduction with Carbon Monoxide. *Anal. Chem.* **1983,** 55, 1980-1986.

(15) Corma, A.; Garcia, H. Supported Gold Nanoparticles as Catalysts for Organic Reactions. *Chem. Soc. Rev.* **2008,** 37, 2096-2126.

(16) Tsunoyama, H.; Ichikuni, N.; Sakurai, H.; Tsukuda, T., Effect of electronic structures of Au clusters stabilized by poly (N-vinyl-2-pyrrolidone) on aerobic oxidation catalysis. *J. Am. Chem. Soc.* **2009,** *131* (20), 7086-7093.

(17) Tsunoyama, H.; Ichikuni, N.; Tsukuda, T. Microfluidic Synthesis and Catalytic Application of PVP-Stabilized,~ 1 nm Gold Clusters. *Langmuir* **2008,** 24, 11327-11330.

(18) Janssens, T. V.; Carlsson, A.; Puig-Molina, A.; Clausen, B. S. Relation Between Nanoscale Au Particle Structure and Activity for CO Oxidation on Supported Gold Catalysts. *J. Catal.* **2006,** 240, 108-113.

(19) Green, I. X.; Tang, W.; Neurock, M.; Yates, J. T. Spectroscopic Observation of Dual Catalytic Sites During Oxidation of CO on a Au/TiO_2 Catalyst. *Science* **2011,** 333, 736-739.

(20) Ferrando, R.; Jellinek, J.; Johnston, R. L. Nanoalloys: from Theory to Applications of Alloy Clusters and Nanoparticles. *Chem. Rev.* **2008,** 108, 845-910.

(21) Chaki, N. K.; Tsunoyama, H.; Negishi, Y.; Sakurai, H.; Tsukuda, T. Effect of Ag-Doping on the Catalytic Activity of Polymer-Stabilized Au Clusters in Aerobic Oxidation of Alcohol. *J. Phys. Chem. C* **2007,** 111, 4885-4888.

(22) Marx, S.; Baiker, A. Beneficial Interaction of Gold and Palladium in Bimetallic Catalysts for the Selective Oxidation of Benzyl Alcohol. *J. Phys. Chem. C* **2009,** 113, 6191-6201.

(23) Tsen, S.-C.; Crozier, P.; Liu, J. Lattice Measurement and Alloy Compositions in Metal and Bimetallic Nanoparticles. *Ultramicroscopy* **2003,** 98, 63-72.

(24) Hanrieder, E. K.; Jentys, A.; Lercher, J. A. Atomistic Engineering of Catalyst Precursors: Dynamic Reordering of PdAu Nanoparticles During Vinyl Acetate Synthesis Enhanced by Potassium Acetate. *ACS Catal.* **2015,** 5, 5776-5786.

(25) Han, Y.-F.; Wang, J.-H.; Kumar, D.; Yan, Z.; Goodman, D. A Kinetic Study of Vinyl Acetate Synthesis over Pd-Based Catalysts: Kinetics of Vinyl Acetate Synthesis over $Pd–Au/SiO_2$ and Pd/SiO_2 Catalysts. *J. Catal.* **2005,** 232, 467-475.

(26) Edwards, J. K.; Solsona, B. E.; Landon, P.; Carley, A. F.; Herzing, A.; Kiely, C. J.; Hutchings, G. J. Direct Synthesis of Hydrogen Peroxide from H_2 and O_2 Using TiO_2-Supported Au–Pd Catalysts. *J. Catal.* **2005,** 236, 69-79.

(27) Edwards, J. K.; Solsona, B.; Ntainjua, E.; Carley, A. F.; Herzing, A. A.; Kiely, C. J.; Hutchings, G. J. Switching off Hydrogen Peroxide Hydrogenation in the Direct Synthesis Process. *Science* **2009,** 323, 1037-1041.

(28) Edwards, J. K.; Freakley, S. J.; Carley, A. F.; Kiely, C. J.; Hutchings, G. J. Strategies for Designing Supported Gold–Palladium Bimetallic Catalysts for the Direct Synthesis of Hydrogen Peroxide. *Acc. Chem. Res.* **2013,** 47, 845-854.

(29) Dimitratos, N.; Lopez-Sanchez, J. A.; Hutchings, G. J. Selective Liquid Phase Oxidation with Supported Metal Nanoparticles. *Chem. Sci.* **2012,** 3, 20-44.

(30) Griffin, M. B.; Rodriguez, A. A.; Montemore, M. M.; Monnier, J. R.; Williams, C. T.; Medlin, J. W. The Selective Oxidation of Ethylene Glycol and 1, 2-Propanediol on Au, Pd, and Au–Pd Bimetallic Catalysts. *J. Catal.* **2013,** 307, 111-120.

(31) Davis, S. E.; Ide, M. S.; Davis, R. J. Selective Oxidation of Alcohols and Aldehydes over Supported Metal Nanoparticles. *Green Chem.* **2013,** 15, 17-45.

(32) Ksar, F.; Ramos, L.; Keita, B.; Nadjo, L.; Beaunier, P.; Remita, H. Bimetallic Palladium–Gold Nanostructures: Application in Ethanol Oxidation. *Chem. Mater.* **2009,** 21, 3677-3683.

(33) Collins, N. R.; Twigg, M. V. Three-Way Catalyst Emissions Control Technologies for Spark-Ignition Engines—Recent Trends and Future Developments. *Top. Catal.* **2007,** 42, 323-332.

(34) Xu, J.; White, T.; Li, P.; He, C.; Yu, J.; Yuan, W.; Han, Y.-F. Biphasic Pd–Au Alloy Catalyst for Low-Temperature CO Oxidation. *J. Am. Chem. Soc.* **2010,** 132, 10398-10406.

(35) Venezia, A.; Liotta, L.; Pantaleo, G.; La Parola, V.; Deganello, G.; Beck, A.; Koppány, Z.; Frey, K.; Horvath, D.; Guczi, L. Activity of SiO_2 Supported Gold-Palladium Catalysts in CO Oxidation. *Appl. Catal. A Gen.* **2003,** 251, 359-368.

(36) Gao, F.; Wang, Y.; Goodman, D. W. CO Oxidation over AuPd (100) from Ultrahigh Vacuum to near-Atmospheric Pressures: the Critical Role of Contiguous Pd Atoms. *J. Am. Chem. Soc.* **2009,** 131, 5734-5735.

(37) Ishizaka, T.; Ishigaki, A.; Kawanami, H.; Suzuki, A.; Suzuki, T. M. Dynamic Control of Gold Nanoparticle Morphology in a Microchannel Flow Reactor by Glucose Reduction in Aqueous Sodium Hydroxide Solution. *J. Colloid Interface Sci.* **2012,** 367, 135-138.

(38) Köhler, J.; Abahmane, L.; Wagner, J.; Albert, J.; Mayer, G. Preparation of Metal Nanoparticles with Varied Composition for Catalytical Applications in Microreactors. *Chem. Eng. Sci.* **2008,** 63, 5048-5055.

(39) Knauer, A.; Thete, A.; Li, S.; Romanus, H.; Csaki, A.; Fritzsche, W.; Köhler, J. Au/Ag/Au Double Shell Nanoparticles with Narrow Size Distribution Obtained by Continuous Micro Segmented Flow Synthesis. *Chem. Eng. J.* **2011,** 166, 1164-1169.

(40) Hayashi, N.; Sakai, Y.; Tsunoyama, H.; Nakajima, A. Development of Ultrafine Multichannel Microfluidic Mixer for Synthesis of Bimetallic Nanoclusters: Catalytic Application of Highly Monodisperse AuPd Nanoclusters Stabilized by Poly (N-vinylpyrrolidone). *Langmuir* **2014,** 30, 10539-10547.

(41) Tofighi, G.; Gaur, A.; Doronkin, D. E.; Lichtenberg, H.; Wang, W.; Wang, D.; Rinke, G.; Ewinger, A.; Dittmeyer, R.; Grunwaldt, J.-D. Microfluidic Synthesis of Ultrasmall AuPd Nanoparticles with a Homogeneously Mixed Alloy Structure in Fast Continuous Flow for Catalytic Applications. *J. Phys. Chem. C* **2018,** 122, 1721-1731.

(42) Tofighi, G. A Microfluidic Reactor for Time and Spatially Resolved in situ Spectroscopic Studies on Nanoparticles During Synthesis. Ph.D. Dissertation, Karlsruhe Institute of Technology, Germany, 2018.

(43) Yang, C.; Wöll, C. IR Spectroscopy Applied to Metal Oxide Surfaces: Adsorbate Vibrations and Beyond. *Adv. Phys. X* **2017**, 2, 373-408.

(44) Tofighi, G.; Lichtenberg, H.; Pesek, J.; Sheppard, T. L.; Wang, W.; Schottner, L.; Rinke, G.; Dittmeyer, R.; Grunwaldt, J.-D. Continuous Microfluidic Synthesis of Colloidal Ultrasmall Gold Nanoparticles: In Situ Study of the Early Reaction Stages and Application for Catalysis. *React. Chem. Eng.* **2017,** 2, 876-884.

(45) Schneider, C. A.; Rasband, W. S.; Eliceiri, K. W. NIH Image to ImageJ: 25 Years of Image Analysis. *Nat. Methods* **2012,** 9, 671-675.

(46) Zimina, A.; Dardenne, K.; Denecke, M. A.; Doronkin, D. E.; Huttel, E.; Lichtenberg, H.; Mangold, S.; Pruessmann, T.; Rothe, J.; Spangenberg, T.; Steininger, R.; Vitova, T.; Geckeis, H.; Grunwaldt, J.-D. CAT-ACT—A New Highly Versatile X-Ray Spectroscopy Beamline for Catalysis and Radionuclide Science at the KIT Synchrotron Light Facility ANKA. *Rev. Sci. Instrum.* **2017,** 88, 113113.

(47) Ravel, B.; Newville, M. ATHENA, ARTEMIS, HEPHAESTUS: Data Analysis for X-Ray Absorption Spectroscopy Using IFEFFIT. *J. Synchrotron Radiat.* **2005,** 12, 537-541.

(48) Wang, Y.; Wöll, C. IR Spectroscopic Investigations of Chemical and Photochemical Reactions on Metal Oxides: Bridging the Materials Gap. *Chem. Soc. Rev.* **2017,** 46, 1875-1932.

(49) Yu, X.; Zhang, Z.; Yang, C.; Bebensee, F.; Heissler, S.; Nefedov, A.; Tang, M.; Ge, Q.; Chen, L.; Kay, B. D. Interaction of Formaldehyde with the Rutile TiO_2 (110) Surface: A Combined Experimental and Theoretical Study. *J. Phys. Chem. C* **2016,** 120, 12626-12636.

(50) Doniach, S.; Sunjic, M. Many-Electron Singularity in X-Ray Photoemission and X-Ray Line Spectra from Metals. *J. Phys. C Solid State Phys.* **1970,** 3, 285.

(51) Scofield, J. H. Hartree-Slater Subshell Photoionization Cross-Sections at 1254 and 1487 eV. *J. Electron Spectrosc. and Related Phenomena* **1976,** 8, 129-137.

(52) Maeland, A.; Flanagan, T. B. Lattice Spacings of Gold–Palladium Alloys. *Can. J. Phys.* **1964,** 42, 2364-2366.

(53) Liu, C.; Chen, N.; Li, J.; Gao, X.; Sham, T.-K.; Wang, S.-D. Fingerprint Feature of Atomic Intermixing in Supported AuPd Nanocatalysts Probed by X-Ray Absorption Fine Structure. *J. Phys. Chem. C* **2017,** 121, 28385-28394.

(54) Arrigo, R.; Schuster, M. E.; Abate, S.; Wrabetz, S.; Amakawa, K.; Teschner, D.; Freni, M.; Centi, G.; Perathoner, S.; Hävecker, M. Dynamics of Palladium on Nanocarbon in the Direct Synthesis of H_2O_2. *ChemSusChem* **2014,** 7, 179-194.

(55) Wang, H.-F.; Kaden, W. E.; Dowler, R.; Sterrer, M.; Freund, H.-J. Model Oxide-Supported Metal Catalysts–Comparison of Ultrahigh Vacuum and Solution Based Preparation of Pd Nanoparticles on a Single-Crystalline Oxide Substrate. *Phys. Chem. Chem. Phys.* **2012,** 14, 11525-11533.

(56) Zemlyanov, D.; Aszalos-Kiss, B.; Kleimenov, E.; Teschner, D.; Zafeiratos, S.; Hävecker, M.; Knop-Gericke, A.; Schlögl, R.; Gabasch, H.; Unterberger, W. In Situ XPS Study of Pd (111) Oxidation. Part 1: 2D Oxide Formation in 10^{-3} mbar O_2. *Surf. Sci.* **2006,** 600, 983-994.

(57) Gabasch, H.; Unterberger, W.; Hayek, K.; Klötzer, B.; Kleimenov, E.; Teschner, D.; Zafeiratos, S.; Hävecker, M.; Knop-Gericke, A.; Schlögl, R. In Situ XPS Study of Pd (111) Oxidation at Elevated Pressure, Part 2: Palladium Oxidation in the 10^{-1} mbar Range. *Surf. Sci.* **2006,** 600, 2980-2989.

(58) Rodriguez, J.; Goodman, D. W. The Nature of the Metal-Metal Bond in Bimetallic Surfaces. *Science* **1992,** 257, 897-903.

(59) Li, Z.; Gao, F.; Furlong, O.; Tysoe, W. T. Adsorption of Carbon Monoxide Au/Pd (100) Alloys in Ultrahigh Vacuum: Identification of Adsorption Sites. *Surf. Sci.* **2010,** 604, 136-143.

(60) Li, Z.; Gao, F.; Wang, Y.; Calaza, F.; Burkholder, L.; Tysoe, W. T. Formation and Characterization of Au/Pd Surface Alloys on Pd (111). *Surf. Sci.* **2007,** 601, 1898-1908.

(61) Gao, F.; Goodman, D. W. Pd–Au Bimetallic Catalysts: Understanding Alloy Effects from Planar Models and (Supported) Nanoparticles. *Chem. Soc. Rev.* **2012,** 41, 8009-8020.

(62) Rodriguez, J. Physical and Chemical Properties of Bimetallic Surfaces. *Surf. Sci. Rep.* **1996,** 24, 223-287.

(63) Lee, Y.-S.; Jeon, Y.; Chung, Y.-D.; Lim, K.-Y.; Whang, C.-N.; Oh, S.-J. Charge Redistribution and Electronic Behavior in Pd-Au Alloys. *J. Korean Phys. Soc.* **2000,** 37, 451-455.

(64) Wang, D.; Cui, X.; Xiao, Q.; Hu, Y.; Wang, Z.; Yiu, Y. M.; Sham, T. K. Electronic Behaviour of Au-Pt Alloys and the 4f Binding Energy Shift Anomaly in Au Bimetallics-X-Ray Spectroscopy Studies. *AIP Adv*. **2018,** 8, 065210.

(65) Xu, M.; Noei, H.; Fink, K.; Muhler, M.; Wang, Y.; Wöll, C. The Surface Science Approach for Understanding Reactions on Oxide Powders: the Importance of IR Spectroscopy. *Angew. Chem. Int. Ed.* **2012,** 51, 4731-4734.

(66) Redhead, P. Thermal Desorption of Gases. *Vacuum* **1962,** 12, 203-211.

(67) Buchholz, M.; Yu, X.; Yang, C.; Heißler, S.; Nefedov, A.; Wang, Y.; Wöll, C. IR-Spectroscopy of CO Adsorption on Mixed-Terminated ZnO Surfaces. *Surf. Sci.* **2016,** 652, 247-252.

(68) Noei, H.; Birkner, A.; Merz, K.; Muhler, M.; Wang, Y. Probing the Mechanism of Low-Temperature CO Oxidation on Au/ZnO Catalysts by Vibrational Spectroscopy. *J. Phys. Chem. C* **2012,** 116, 11181-11188.

(69) Wang, Y.; Xia, X.; Urban, A.; Qiu, H.; Strunk, J.; Meyer, B.; Muhler, M.; Wöll, C. Tuning the Reactivity of Oxide Surfaces by Charge-Accepting Adsorbates. *Angew. Chem. Int. Ed.* **2007,** 46, 7315-7318.

(70) Meier, D. C.; Goodman, D. W. The Influence of Metal Cluster Size on Adsorption Energies: CO Adsorbed on Au Clusters Supported on TiO_2. *J. Am. Chem. Soc.* **2004,** 126, 1892-1899.

(71) Dekkers, M.; Lippits, M.; Nieuwenhuys, B. CO Adsorption and Oxidation on Au/TiO_2. *Catal. Lett.* **1998,** 56, 195-197.

(72) Grunwaldt, J.-D.; Maciejewski, M.; Becker, O. S.; Fabrizioli, P.; Baiker, A. Comparative Study of Au/TiO_2 and Au/ZrO_2 Catalysts for Low-Temperature CO Oxidation. *J. Catal.* **1999,** 186, 458-469.

(73) Boccuzzi, F.; Chiorino, A.; Manzoli, M. FTIR Study of the Electronic Effects of CO Adsorbed on Gold Nanoparticles Supported on Titania. *Surf. Sci.* **2000,** 454, 942-946.

(74) Hartshorn, H.; Pursell, C. J.; Chandler, B. D. Adsorption of CO on Supported Gold Nanoparticle Catalysts: a Comparative Study. *J. Phys. Chem. C* **2009,** 113, 10718-10725.

(75) Yang, C.; Yu, X.; Heißler, S.; Nefedov, A.; Colussi, S.; Llorca, J.; Trovarelli, A.; Wang, Y.; Wöll, C. Surface Faceting and Reconstruction of Ceria Nanoparticles. *Angew. Chem. Int. Ed.* **2017,** 56, 375-379.

(76) Abbott, H. L.; Aumer, A.; Lei, Y.; Asokan, C.; Meyer, R. J.; Sterrer, M.; Shaikhutdinov, S.; Freund, H.-J. CO Adsorption on Monometallic and Bimetallic Au–Pd Nanoparticles Supported on Oxide Thin Films. *J. Phys. Chem. C* **2010,** 114, 17099-17104.

(77) Crossley, A.; King, D. A. Infrared Spectra for CO Isotopes Chemisorbed on Pt "111": Evidence for Strong Absorbate Coupling Interactions. *Surf. Sci.* **1977,** 68, 528-538.

(78) Persson, B.; Ryberg, R. Vibrational Interaction Between Molecules Adsorbed on a Metal Surface: the Dipole-Dipole Interaction. *Phys. Rev. B* **1981,** 24, 6954.

(79) Muglali, M. I.; Liu, J.; Bashir, A.; Borissov, D.; Xu, M.; Wang, Y.; Wöll, C.; Rohwerder, M. On the Complexation Kinetics for Metallization of Organic Layers: Palladium onto a Pyridine-Terminated Araliphatic Thiol Film. *Phys. Chem. Chem. Phys.* **2012**, 14, 4703-4712.

(80) Wang, G.; Wang, H.; Ling, Y.; Tang, Y.; Yang, X.; Fitzmorris, R. C.; Wang, C.; Zhang, J. Z.; Li, Y. Hydrogen-Treated TiO_2 Nanowire Arrays for Photoelectrochemical Water Splitting. *Nano Lett.* **2011,** 11, 3026-3033.

(81) Wendt, S.; Schaub, R.; Matthiesen, J.; Vestergaard, E. K.; Wahlström, E.; Rasmussen, M. D.; Thostrup, P.; Molina, L.; Lægsgaard, E.; Stensgaard, I. Oxygen Vacancies on TiO_2 (110) and their Interaction with H_2O and O_2: a Combined High-Resolution STM and DFT Study. *Surf. Sci.* **2005,** 598, 226-245.

(82) Lang, S. M.; Fleischer, I.; Bernhardt, T. M.; Barnett, R. N.; Landman, U. Low-Temperature CO Oxidation Catalyzed by Free Palladium Clusters: Similarities and Differences to Pd Surfaces and Supported Particles. *ACS Catal.* **2015,** 5, 2275-2289.

(83) Song, W.; Su, Y.; Hensen, E. J. A DFT Study of CO Oxidation at the Pd–CeO_2 (110) Interface. *J. Phys. Chem. C* **2015,** 119, 27505-27511.

(84) Kunz, S.; Schweinberger, F. F.; Habibpour, V.; Röttgen, M.; Harding, C.; Arenz, M.; Heiz, U. Temperature Dependent CO Oxidation Mechanisms on Size-Selected Clusters. *J. Phys. Chem. C* **2009,** 114, 1651-1654.

(85) Kim, H. Y.; Lee, H. M.; Henkelman, G. CO Oxidation Mechanism on CeO_2-Supported Au Nanoparticles. *J. Am. Chem. Soc.* **2012,** 134, 1560-1570.

(86) Song, W.; Hensen, E. J. A Computational DFT Study of CO Oxidation on a Au Nanorod Supported on CeO_2 (110): on the Role of the Support Termination. *Catal. Sci. Technol.* **2013,** 3, 3020-3029.

(87) Zhang, J.; Alexandrova, A. N. The Golden Crown: a Single Au Atom that Boosts the CO Oxidation Catalyzed by a Palladium Cluster on Titania Surfaces. *J. Phys. Chem. Lett.* **2013,** 4, 2250-2255.

(88) Lang, S. M.; Fleischer, I.; Bernhardt, T. M.; Barnett, R. N.; Landman, U. Size-Dependent Self-Limiting Oxidation of Free Palladium Clusters. *J. Phys. Chem. A* **2014,** 118, 8572-8582.

(89) Zhou, Y.; Doronkin, D. E.; Chen, M.; Wei, S.; Grunwaldt, J.-D. Interplay of Pt and Crystal Facets of TiO_2: CO Oxidation Activity and Operando XAS/DRIFTS Studies. *ACS Catal.* **2016,** 6, 7799-7809.

(90) Yogi, C.; Kojima, K.; Hashishin, T.; Wada, N.; Inada, Y.; Della Gaspera, E.; Bersani, M.; Martucci, A.; Liu, L.; Sham, T.-K. Size Effect of Au Nanoparticles on TiO_2 Crystalline Phase of NanoComposite Thin Films and their Photocatalytic Properties. *J. Phys. Chem. C* **2011,** 115, 6554-6560.

Table of Contents artwork